ChemComm

COMMUNICATION

View Article Online
View Journal | View Issue

Cite this: *Chem. Commun.*, 2026, **62**, 7329

Received 15th January 2026,
Accepted 12th March 2026

DOI: 10.1039/d6cc00289g

rsc.li/chemcomm

A MoO_3–CoOOH synergistic catalyst for low-voltage paired glycerol electrolysis

Genxiang Wang,[ab] Pengzhen Zhang,[a] Jun Wang,[b] Junfeng Wang,[a] Xiang Hu,[b] Zhiwen Lu,[b] Jing Yang,*[ac] Zhenhai Wen*[b] and Hao Zhang*[de]

A synergistic MoO_3–$Co(OH)_2$ precatalyst achieves efficient glycerol oxidation to formate in alkaline media, where *in situ* formed CoOOH serves as the active phase and MoO_3 enhances glycerol adsorption. Coupling this anodic reaction with an acidic HER in a hybrid electrolyzer achieves concurrent formate and H_2 production at a voltage of 0.44 V.

Traditional chemical synthesis heavily relies on fossil resources under harsh conditions, leading to high energy consumption and environmental issues. In contrast, electrochemical synthesis, powered by renewable electricity under ambient conditions, offers a sustainable alternative for producing value-added chemicals and storing intermittent energy.[1–3] Glycerol, an abundant byproduct of biodiesel production, is an ideal platform molecule for electrochemical upgrading due to its low cost and versatile chemistry.[4] The electrochemical glycerol oxidation reaction (GOR) can yield valuable products like glyceric acid, dihydroxyacetone, and formic acid, with the latter being a valuable hydrogen carrier and industrial feedstock.[5,6] Moreover, replacing the oxygen evolution reaction (OER) with the GOR in electrolyzers can significantly lower the energy input for processes like hydrogen evolution and enable the co-production of chemicals.[6] Despite its potential, the GOR involves complex multi-electron pathways, making the development of catalysts with high activity and selectivity a major challenge.

Significant research efforts have been dedicated to designing advanced catalysts for this purpose. While noble metal catalysts show promise, their cost and susceptibility to poisoning drive the search for Earth-abundant alternatives.[7,8] Cobalt-based materials are promising candidates due to their tunable electronic structures and rich redox chemistry in alkaline media.[9,10] Strategies such as doping and forming heterostructures with secondary metals (*e.g.*, Ni, Mn, and Cu) have been employed to enhance their selectivity and activity by promoting the formation of active CoOOH species and modulating intermediate adsorption.[11–14] Notably, introducing high-valence metals like Mo^{6+} can withdraw electrons from Co, promoting the formation of Co^{3+} and offering a promising yet under-explored avenue for improving GOR catalysts.[10,15]

Herein, a hybrid MoO_3–$Co(OH)_2$ precatalyst grown on carbon cloth (MoO_3–$Co(OH)_2$/CC) was developed as an efficient GOR electrocatalyst, which requires only 1.20 V against the reversible hydrogen electrode (*vs.* RHE) to achieve 10 mA cm^{-2} and maintains over 90% faradaic efficiency for formate from 1.25 to 1.45 V. Combined experimental and theoretical studies confirm that *in situ* formed CoOOH serves as the active site, while Mo^{6+} enhances glycerol adsorption. Furthermore, a hybrid alkaline–acid electrolyzer with this anode and a Pt/C cathode achieves 10 mA cm^{-2} at a cell voltage of only 0.44 V, saving over 65% energy compared to conventional water electrolysis and enabling the green co-production of formate and hydrogen.

To incorporate high-valence Mo^{6+} into Co-based catalysts, a modified one-step electrodeposition method was used to prepare a MoO_3–$Co(OH)_2$/CC hybrid grown *in situ* on carbon cloth.[16] X-ray diffraction (XRD) patterns (Fig. 1a) show distinct diffraction peaks for pure $Co(OH)_2$.[17] In contrast, for the MoO_3–$Co(OH)_2$/CC sample, the intensity of the $Co(OH)_2$ peaks significantly decreases, and no distinct diffraction peaks corresponding to Mo-containing phases are observed. This indicates that Mo incorporation affects the crystallinity of $Co(OH)_2$, and the Mo species likely exist in a low-crystalline or amorphous state.[16,18,19] The XRD pattern and the high-resolution transmission electron microscopy (HRTEM) image of the controlled sample MoO_3/CC display only the broad peaks of the carbon cloth and no obvious lattice fringes, further confirming its low-crystalline or amorphous structure (Fig. S1). Scanning electron microscopy (SEM) and TEM

[a] *School of Energy and Power Engineering, Jiangsu University, Zhenjiang, 212013, China. E-mail: jingyang@ujs.edu.cn*
[b] *Fujian Institute of Research on the Structure of Matter, Chinese Academy of Sciences, Fuzhou, Fujian, 350002, China. E-mail: wen@fjirsm.ac.cn*
[c] *Department of Applied Biology and Chemical Technology, The Hong Kong Polytechnic University, Hung Hom, Hong Kong S.A.R, China*
[d] *State Key Laboratory of Chem/Bio-Sensing and Chemometrics, College of Chemistry and Chemical Engineering, Hunan University, Changsha 410082, China. E-mail: hzhchem@mit.edu*
[e] *Department of Chemical Engineering, Massachusetts Institute of Technology, Cambridge, MA 02139, USA*

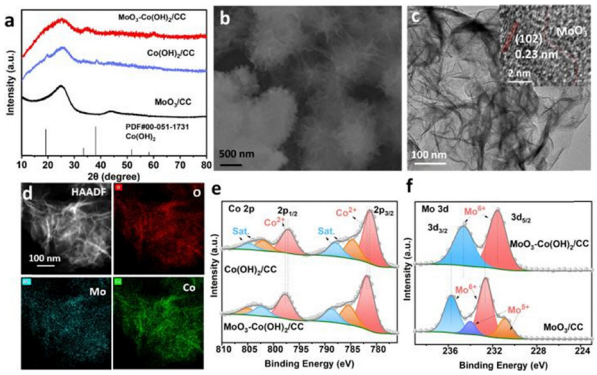

Fig. 1 Characterization of MoO_3–$Co(OH)_2$/CC. XRD patterns (a), SEM image (b), TEM image and HRTEM image (inset) (c), energy-dispersive spectroscopic mapping images (d), and high-resolution XPS spectra of Co 2p (e) and Mo 3d (f).

images reveal that MoO_3–$Co(OH)_2$/CC possesses a three-dimensional porous nanoflower architecture composed of interconnected wrinkled nanosheets with a thickness of approximately 4–5 nm (Fig. 1b, c and Fig. S2, S3). The HRTEM image shows discernible lattice fringes with an interplanar spacing of 0.23 nm, corresponding to the (102) plane of $Co(OH)_2$, alongside amorphous regions attributed to the MoO_3 phase,[16] indicating a heterointerface formed between amorphous MoO_3 and crystalline $Co(OH)_2$ (Fig. 3c and d). Energy dispersive spectroscopy (EDS) mapping confirms the uniform distribution of Co, Mo, and O throughout the nanosheets (Fig. 1d). Furthermore, inductively coupled plasma optical emission spectroscopy (ICP-OES) analysis confirmed that the Mo : Co ratio in the prepared electrode was 2.8 : 1, relatively close to the input ratio used during synthesis.

X-ray photoelectron spectroscopy (XPS) analysis (Fig. 1e, f and Fig. S4) elucidated the surface composition and interfacial electronic interaction in the MoO_3–$Co(OH)_2$/CC hybrid. The survey spectrum confirmed the presence of Co, Mo, and O (Fig. S4a). In the high-resolution spectra, Co 2p peaks at 781.9 and 797.7 eV were assigned to Co^{2+} (Fig. 1e), while Mo 3d peaks at 231.5 and 234.6 eV indicated the presence of Mo^{6+} (Fig. 1f).[16,18,20] Compared to pure $Co(OH)_2$/CC, the Co 2p binding energy in the hybrid exhibited a positive shift, while pure MoO_3/CC showed a mixed Mo^{6+} and Mo^{5+} state.[10,21,22] The distinct Mo valence states observed in the pure MoO_3/CC and the MoO_3–$Co(OH)_2$/CC hybrid are directly linked to the formation of a heterointerface in the latter. In the pure MoO_3/CC sample, the cathodic electrodeposition process can partially reduce Mo^{6+} precursors to Mo^{5+}, resulting in a mixed-valence state.[16,23] In contrast, the electronic structure is reconfigured in the MoO_3–$Co(OH)_2$ hybrid. The concurrent positive shift in the Co 2p binding energy and negative shift in the Mo 3d binding energy (Fig. 1e and f) provide direct evidence of electron transfer from Co to Mo across this heterointerface. This electron donation stabilizes the Mo^{6+} oxidation state by satisfying its inherent electron demand, making it thermodynamically less susceptible to reduction during synthesis. Consequently, Mo remains predominantly in the +6 state in the hybrid structure, while the electronic interaction is conducive to promoting the formation of Co^{3+} species, which are beneficial for the GOR.[18]

Linear scanning voltammetry (LSV) was performed to evaluate the OER and GOR activities of the catalysts in 1.0 M KOH with and without 0.5 M glycerol (Fig. 2). The MoO_3–$Co(OH)_2$/CC hybrid required only 1.20 V *vs.* RHE to achieve 10 mA cm^{-2} for the GOR, which is 290 mV lower than its OER potential (1.49 V) and significantly lower than the potentials needed for $Co(OH)_2$/CC and inactive MoO_3/CC (Fig. S5 and Fig. 2a). Moreover, compared to $Co(OH)_2$/CC, the overpotentials of the MoO_3–$Co(OH)_2$/CC hybrid were reduced by 100, 60, and 110 mV at 10, 50, and 100 mA cm^{-2}, respectively (Fig. S5b). Additionally, MoO_3–$Co(OH)_2$/CC exhibited a lower Tafel slope (47.5 mV dec^{-1}) and smaller charge transfer resistance than the control samples, indicating superior reaction kinetics and facilitated electron transfer (Fig. 2b and c). While its double-layer capacitance (9.7 mF cm^{-2}) was slightly lower than that of $Co(OH)_2$/CC (9.8 mF cm^{-2}) (Fig. S5c–g), the enhanced performance suggests that Mo incorporation improves intrinsic activity. Product analysis by ^{1}H nuclear magnetic resonance (^{1}H NMR) identified formate as the primary product, with a faradaic efficiency exceeding 90% within 1.25–1.45 V *vs.* RHE and peaking at 98.2% at 1.35 V, accompanied by minor amounts of dihydroxyacetone (DHA) and glyceraldehyde (GLAD) (Fig. 2d and Fig. S6 and S7).[24] Chronopotentiometry at 10 mA cm^{-2} confirmed stable operation for 120 h. Post-stability characterization (XPS, XRD, and SEM) revealed morphological preservation but Mo loss, along with phase transformation to CoOOH and the

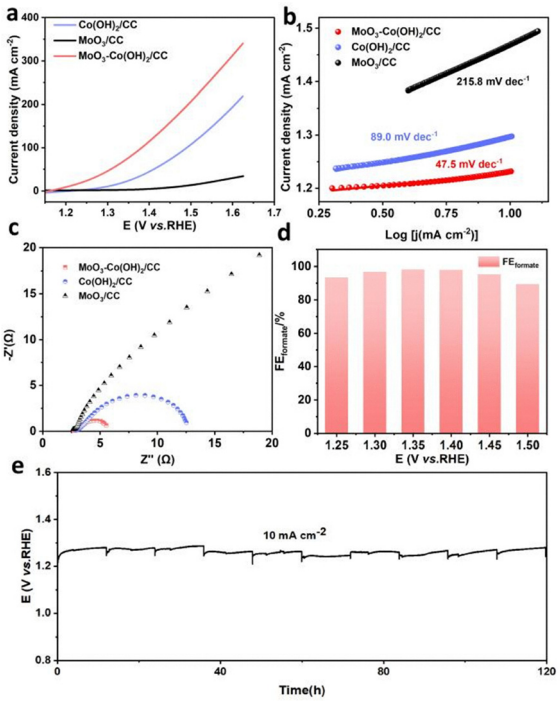

Fig. 2 The electrochemical performance characterization. (a) LSV curves of the GOR over different samples, (b) Tafel curves derived from Fig. 2a, (c) Nyquist plots at 1.4 V *vs.* RHE for the GOR, (d) formate faradaic efficiency under different potentials, and (e) the long-term stability test of MoO_3–$Co(OH)_2$/CC with a refreshing electrolyte every 12 hours.

presence of Co^{3+} and Mo^{6+}, confirming catalyst reconstruction during the GOR (Fig. S8 and S9).[22,25] Overall, the GOR performance of the prepared catalyst is competitive with these reported works (Table S1).

Deeper insight into the surface structural evolution of MoO_3–$Co(OH)_2$/CC during the OER and GOR processes was then investigated by *in situ* Raman spectroscopy. In the 1.0 M KOH electrolyte, characteristic CoOOH peaks (~486, 525, and 688 cm^{-1}) emerged at 1.324 V *vs.* RHE, confirming the oxidation of Co^{2+} to Co^{3+}.[26,27] Their intensity decreased at 1.524 V, indicating CoOOH consumption during the OER (Fig. S10). Notably, the surface of MoO_3–$Co(OH)_2$ was almost transformed into MoO_3–CoOOH after the OER. Therefore, when the same electrode was directly used for GOR tests, distinct CoOOH peaks were already present. As the potential increased to 1.124 V, these peak intensities diminished continuously up to 1.524 V (Fig. 3a), suggesting that the GOR initiates around 1.124 V and then rapidly consumes the formed CoOOH active sites within this potential window. These observations agree well with the absence of a distinct Co^{3+} oxidation peak in the GOR LSV curve. In addition, *operando* electrochemical impedance spectroscopy (EIS) was further conducted to probe the interfacial electrochemical behavior of MoO_3–$Co(OH)_2$/CC, $Co(OH)_2$/CC and MoO_3/CC during the GOR and OER (Fig. 3b and Fig. S11–S13).[9,13] During the OER process of MoO_3–$Co(OH)_2$/CC, a phase angle peak (inflection point) appears in the low-frequency region when the potential increases to 1.55 V *vs.* RHE, likely associated with the hydroxyl adsorption and initiation of oxidation reactions (Fig. S11b).[13] The potential is close to the potential at which the OER starts to occur. In the presence of glycerol, a similar phase angle peak appeared around 1.25 V *vs.* RHE in the low-frequency region of the Bode curve, corresponding to the large semicircle in the Nyquist curve (Fig. 3b and Fig. S11c). This indicates that hydroxyl groups may be involved in the GOR process. As the potential increases, the phase angle peak slowly shifts toward higher frequencies and lower phase angle values, suggesting that the adsorbed glycerol molecules are rapidly oxidized, leading to faster interfacial charge transfer. Although $Co(OH)_2$/CC exhibited similar trends to those of MoO_3–$Co(OH)_2$/CC during the OER and GOR processes, its phase angle peak value is higher than that of MoO_3–$Co(OH)_2$/CC, indicating that the introduction of Mo results in a higher reaction rate. Therefore, the *operando* EIS test results are consistent with the LSV measurements and confirm the excellent GOR performance of MoO_3–$Co(OH)_2$/CC. Besides, the competitive adsorption between hydroxide ions and glycerol was revealed by measuring LSV curves of MoO_3–$Co(OH)_2$/CC and $Co(OH)_2$/CC in GOR electrolytes with varying KOH concentrations (with 0.5 M glycerol). Fig. S14a and b showed higher KOH concentrations reduced the potential required to achieve the same current density for both MoO_3–$Co(OH)_2$/CC and $Co(OH)_2$/CC. The GOR current density at 1.45 V *vs.* RHE exhibited a linear relationship with KOH concentration (0.1–1.0 M), implying their comparable OH* adsorption capacity.[13] At higher concentrations (>1.0 M), competition between glycerol and OH* causes more active sites occupied by OH*, inhibiting glycerol adsorption and reducing current density. The MoO_3–$Co(OH)_2$/CC possesses a higher slope (112.6) than $Co(OH)_2$/CC (92.7), indicating its faster GOR kinetics.[28] To further examine glycerol adsorption, kinetic measurements were performed by recording LSV curves in 1 M KOH with varying glycerol concentrations (Fig. S14c–e). For $Co(OH)_2$/CC, the current density gradually increased from 0.1 to 0.8 M, with a reaction order of 0.336 (Fig. S14e, inset). At higher concentrations (0.8–1.0 M), the current density peaked at ~109 mA cm^{-2}, suggesting adsorption saturation. In contrast, MoO_3–$Co(OH)_2$/CC delivered higher current densities with a lower reaction order of 0.239, implying that the reaction rate depends less on glycerol concentration, consistent with enhanced adsorption on the MoO_3 modified surface. The peak current density reached 141 mA cm^{-2} at a lower glycerol concentration (0.7 M), further confirming easier saturation on MoO_3–$Co(OH)_2$/CC.[8,29]

To clarify the role of Mo, density functional theory (DFT) calculations were performed on a MoO_3–CoOOH heterostructure model, guided by the experimental identification of CoOOH as the active phase.[30] Differential charge analysis reveals strong electron interactions at the MoO_3–CoOOH heterointerface (Fig. S15). The density of states (DOS) analysis indicates that the d-band center of MoO_3–CoOOH (−1.22 eV) shifts positively towards the Fermi level compared to CoOOH (−1.26 eV), signifying enhanced adsorption affinity for glycerol molecules (Fig. S14f).[13] To elucidate the reaction mechanism, we computed the Gibbs free energy changes of key intermediates. Based on the

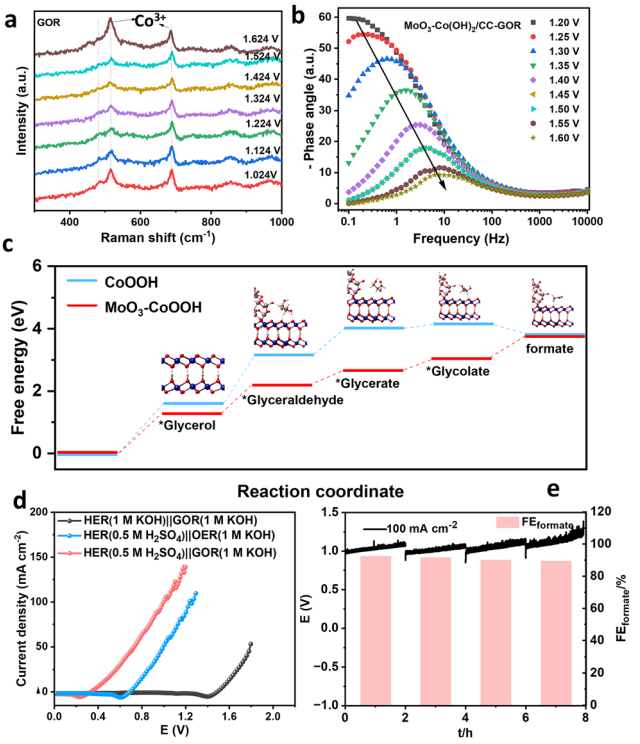

Fig. 3 *In situ* Raman (a) and Bode plots (b) under various potentials for GOR over MoO_3–$Co(OH)_2$/CC, (c) the proposed possible mechanistic pathway of GOR over MoO_3–CoOOH and free energy profiles for GOR at MoO_3–CoOOH and CoOOH, (b) LSV curves of HER||GOR and HER||OER overall electrolysis under different pH difference at scan rate of 5 mV s^{-1}, (b) summary of cell voltage value at different current densities in the asymmetric-electrolyte HER||GOR electrolyzer, (e) four successive electrolysis cycles at 100 mA cm^{-2} with recorded selectivity of formate.

detected liquid product during experiments, the reaction follows the traditional glycerol oxidation pathway, in which glycerol first adsorbs onto the catalyst surface and then undergoes oxidation *via* intermediates such as *glyceraldehyde, *glycerate, and *glycolate, ultimately yielding formate (SI). The free energy diagrams (FED) for the GOR identified the initial glycerol adsorption step as the potential-determining step (PDS) for both catalysts (Fig. 3c and Fig. S16, S17).[31] Crucially, the lower Gibbs energy barrier for this PDS in MoO_3–CoOOH demonstrates that Mo incorporation facilitates glycerol adsorption by reducing the necessary energy input.

Building upon the favorable GOR performance of MoO_3–$Co(OH)_2$/CC, an asymmetric-electrolyte electrolyzer was assembled with MoO_3–$Co(OH)_2$/CC in 1 M KOH containing 0.5 M glycerol paired with Pt/C/CC in 0.5 M H_2SO_4 for the HER, separated by a Nafion 117 membrane (Fig. S18a). In this electrolyzer, glycerol is oxidized to formate at the alkaline anode, releasing electrons to the cathode *via* the external circuit where H^+ is reduced to H_2, with K^+ ions migrating through the cation exchange membrane from the anode to the cathode chamber to complete the circuit. This design harnesses energy from both glycerol oxidation and electrochemical neutralization (ENE = 0.0591ΔpH) (SI).[5,32] The hybrid device achieved a remarkably low cell voltage of only 0.44 V at 10 mA cm^{-2}, far below the 1.57 V required for a symmetric alkaline system (1 M KOH-HER‖1 M KOH-GOR), highlighting the critical role of the pH difference (Fig. 3d). Furthermore, the GOR itself contributes significantly, as the GOR-integrated device operates at potentials 240–320 mV lower than its OER-integrated counterpart at 10–100 mA cm^{-2} (Fig. S18b). Stability tests confirmed robust operation for 12 h at 10 mA cm^{-2} with a cell voltage under 0.5 V and an average $FE_{formate}$ of ∼93.5% (Fig. S18c). Even under higher current density cycling at 100 mA cm^{-2}, $FE_{formate}$ remained stable at ∼90% across four cycles, demonstrating its potential for scalable, dual value-added production (Fig. 3e).

In summary, a MoO_3–$Co(OH)_2$/CC nanosheet precatalyst prepared by electrodeposition achieves efficient glycerol oxidation (1.20 V for 10 mA cm^{-2}) with over 90% formate selectivity. Studies confirm that *in situ* formed CoOOH acts as active sites, while MoO_3 promotes glycerol adsorption. A hybrid alkaline–acid electrolyzer using this anode achieves 10 mA cm^{-2} at only 0.44 V, enabling energy-saving co-production of formate and hydrogen, and offers a viable strategy for green electrochemical synthesis.

Genxiang Wang designed the project and carried out most of the experiments and analysis. Pengzhen Zhang and Jun Wang carried out the EIS and ^1H NMR tests. Junfeng Wang assisted to revise manuscript. Xiang Hu carried out the SEM and TEM tests. Zhiwen Lu carried out the *in situ* Raman tests. Jing Yang carried out the theoretical calculation. Zhenhai Wen and Hao Zhang proposed the concept, revised the manuscript, and provided constructive suggestions. All authors contributed to the organization.

Conflicts of interest

There are no conflicts to declare.

Data availability

The data related to this manuscript have been included as part of the supplementary information (SI). Supplementary information: Fig. S1–S18, Table S1 and further experimental details. See DOI: https://doi.org/10.1039/d6cc00289g.

Acknowledgements

This research was financially supported by the National Natural Science Foundation of China (No. 52436005, 22209183 and 22225902), the National Key Research & Development Program of China (2022YFE0115900), and the Advanced Talents of Jiangsu University, China (Grant No. 23JDG027).

References

1 G. Wang, A. Chen, Y. Chen, F. Qiao, J. Wang, N. Yang, H. Zhang and Z. Wen, *eScience*, 2025, **5**, 100333.
2 Y. Zhou, Y. Liang, Z. Zhao, X. Wang, R. Guan, C. Li, L. Yang, F. Qiao, J. Wang, Z. Wu, Y. Fu and J.-B. Baek, *Nano Energy*, 2025, **144**, 111348.
3 X. Fan, C. Liu, X. He, Z. Li, L. Yue, W. Zhao, J. Li, Y. Wang, T. Li, Y. Luo, D. Zheng, S. Sun, Q. Liu, L. Li, W. Chu, F. Gong, B. Tang, Y. Yao and X. Sun, *Adv. Mater.*, 2024, **36**, 2401221.
4 P. Prabhu, Y. Wan and J.-M. Lee, *Matter*, 2020, **3**, 1162–1177.
5 G. Wang, J. Chen, F. Qiao, J. Wang and Z. Wen, *Chem.Sci.*, 2025, **16**, 12651–12678.
6 X. Hu, J. Lu, Y. Liu, L. Chen, X. Zhang and H. Wang, *Environ. Chem. Lett.*, 2023, **21**, 2825–2861.
7 L. Shen, L. Sun, M. Douthwaite, O. Akdim, S. Taylor and G. J. Hutchings, *ACS Catal.*, 2024, **14**, 11343–11351.
8 Y. Yan, H. Zhou, S.-M. Xu, J. Yang, P. Hao, X. Cai, Y. Ren, M. Xu, X. Kong, M. Shao, Z. Li and H. Duan, *J. Am. Chem. Soc.*, 2023, **145**, 6144–6155.
9 Y. Fang, C. Dai, X. Liu, Y. Wang, C. Ju, S. He, R. Shi, Y. Liu, J. Zhang, Y. Zhu and J. Wang, *Nano Energy*, 2024, **127**, 109754.
10 J. Sun, G. Ren, S. Qin, Z. Zhao, Z. Li, Z. Zhang, C. Li and X. Meng, *Nano Energy*, 2024, **121**, 109246.
11 J. Li, X. Meng, X. Song, J. Qi, F. Liu, X. Xiao, Y. Du, G. Xu, Z. Jiang, S. Ye, S. Huang and J. Qiu, *Adv. Funct. Mater.*, 2024, **34**, 2316718.
12 Y. Zhu, Q. Z. Qian, Y. X. Chen, X. Y. He, X. W. Shi, W. T. Wang, Z. Y. Li, Y. F. Feng, G. Q. Zhang and F. Y. Cheng, *Adv. Funct. Mater.*, 2023, **33**, e2300547.
13 J. Ma, X. Wang, J. Song, Y. Tang, T. Sun, L. Liu, J. Wang, J. Wang and M. Yang, *Angew. Chem., Int. Ed.*, 2024, 63, e202319153.
14 C. Li, H. Li, B. Zhang, H. Li, Y. Wang, X. Wang, P. Das, Y. Li, X. Wu, Y. Li, Y. Cui, J. Xiao and Z. S. Wu, *Angew. Chem., Int. Ed.*, 2024, **63**, 2411542.
15 C. Xu, W. Lu, L. Yan, J. Ning, C. Zheng, Y. Zhong, Z. Zhang and Y. Hu, *J. Colloid Interface Sci.*, 2020, **562**, 400–408.
16 X. Li, Y. Wang, J. Wang, Y. Da, J. Zhang, L. Li, C. Zhong, Y. Deng, X. Han and W. Hu, *Adv. Mater.*, 2020, **32**, e2003414.
17 R. Sukanya, S. Mohandoss, R. Karthik, M. Hasan, J.-J. Shim and Y. R. Lee, *J. Energy Storage*, 2023, **73**, 109000.
18 H. Yang, T. Hu, R. Meng and L. Guo, *J. Solid State Chem.*, 2023, **320**, 123837.
19 Y. Zhou, Y. Liang, Z. Wu, X. Wang, R. Guan, C. Li, F. Qiao, J. Wang, Y. Fu and J. B. Baek, *Small*, 2025, **21**, 2411941.
20 X. Feng, K. Guo, C. Jia, B. Liu, S. Ci, J. Chen and Z. Wen, *Acta Phys. Chim. Sin.*, 2023, **0**, 2303050.
21 C. Li, Z. Wang, M. Liu, E. Wang, B. Wang, L. Xu, K. Jiang, S. Fan, Y. Sun, J. Li and K. Liu, *Nat. Commun.*, 2022, **13**, 3338.
22 Y. Ou, L. Liu, X. Peng, L. Zhang, Z. Ou, W. Zhang and Y. Zhang, *Nano Mater. Sci.*, 2024, **6**, 565–575.
23 H. Li, K. Yu, Z. Tang, H. Fu and Z. Zhu, *Phys. Chem. Chem. Phys.*, 2016, **18**, 14074–14085.
24 P. Wang, K. Chen, J. Chen, G. Wang, W. Pan and Z. Wen, *Adv. Funct. Mater.*, 2024, **34**, 2408267.
25 Y. Li, X. Wei, L. Chen, J. Shi and M. He, *Nat. Commun.*, 2019, **10**, 5335.
26 L. Tang, L. Yu, C. Ma, Y. Song, Y. Tu, Y. Zhang, X. Bo and D. Deng, *J. Mater. Chem. A*, 2022, **10**, 6242–6250.

27 J. Chang, F. Song, Y. Hou, D. Wu, F. Xu, K. Jiang and Z. Gao, *J. Colloid Interface Sci.*, 2024, **665**, 152–162.
28 Z. He, J. Zhang, Z. Gong, H. Lei, D. Zhou, N. Zhang, W. Mai, S. Zhao and Y. Chen, *Nat. Commun.*, 2022, **13**, 2191.
29 E. Habibi and H. Razmi, *Int. J. Hydrogen Energy*, 2012, **37**, 16800–16809.
30 A. A. Peterson, F. Abild-Pedersen, F. Studt, J. Rossmeisl and J. K. Nørskov, *Energy Environ. Sci.*, 2010, **3**, 1311–1315.
31 L. Fan, Y. Ji, G. Wang, Z. Zhang, L. Yi, K. Chen, X. Liu and Z. Wen, *J. Energy Chem.*, 2022, **72**, 424–431.
32 G. Wang, J. Chen, Y. Li, J. Jia, P. Cai and Z. Wen, *Chem. Commun.*, 2018, **54**, 2603–2606.